Science Advances
AAAS

advances.sciencemag.org/cgi/content/full/6/23/eaba3367/DC1

Supplementary Materials for

Continuous angle-tunable birefringence with freeform metasurfaces for arbitrary polarization conversion

Zhujun Shi, Alexander Y. Zhu, Zhaoyi Li, Yao-Wei Huang, Wei Ting Chen, Cheng-Wei Qiu, Federico Capasso*

*Corresponding author. Email: capasso@seas.harvard.edu

Published 3 June 2020, *Sci. Adv.* **6**, eaba3367 (2020)
DOI: 10.1126/sciadv.aba3367

This PDF file includes:

1 Jones matrix analysis

The Jones matrix, i.e. transmission matrix, of a metasurface shape birefringent component is constrained by three conditions: unitarity, reciprocity, and geometrical symmetries. Here we assume that all materials are linear and reciprocal, and that absorption is negligible for the wavelengths of interest. We are going to discuss how these conditions restrict the form of the Jones matrix and the corresponding eigen-polarization states.

1.1 Unitarity

The Jones matrix is proportional to a unitary matrix if there is no dichroism, i.e. the transmission efficiency is polarization-independent. This is usually a good approximation for lossless dielectric metasurfaces away from resonances. Note that here we do not require the system to have unity transmission efficiency, as long as the transmission efficiency is similar for different polarization states. A direct consequence of unitarity is the orthogonality of eigen-polarization states.

1.2 Reciprocity

Reciprocity links the Jones matrix for forward ($J_f = J(\hat{k})$) and reverse ($J_r = J(-\hat{k})$) propagation. Here $\hat{k}$ denotes the light momentum. To understand this, consider time-reversal situations of light transmitting through an unitary polarization elements (Fig. S1). Here $\boldsymbol{a}, \boldsymbol{b}$ and $\boldsymbol{a}^*, \boldsymbol{b}^*$ are two-component complex polarization vectors. When expressed in a fixed global coordinate system, $\boldsymbol{a}$ and $\boldsymbol{a}^*$, (as well as $\boldsymbol{b}$ and$\boldsymbol{b}^*$), are complex conjugate to each other. Fig. S1(a) is expressed as

$$\boldsymbol{b} = J(\hat{k})\boldsymbol{a} \tag{1}$$

Similarly, Fig. S1(b) is expressed as

$$\boldsymbol{a}^* = J(-\hat{k})\boldsymbol{b}^* \tag{2}$$

If J_f is unitary, then equation 1 yields

$$\begin{aligned} &\boldsymbol{b} = J(\hat{k})\boldsymbol{a} \\ \Leftrightarrow\ &(J(\hat{k}))^{-1}\boldsymbol{b} = \boldsymbol{a} \\ \Leftrightarrow\ &(J(\hat{k})^T)\boldsymbol{b}^* = \boldsymbol{a}^* \end{aligned} \tag{3}$$

Compare equation 3 with equation 2, one immediately obtains that

$$J(-\hat{k}) = (J(\hat{k}))^T \tag{4}$$

The above relation is expressed using a fixed global coordinate system ($oxyz$) for both propagation directions. In many cases, it is convenient to use different coordinate systems for forward ($oxyz$, Fig. S1(a)) and reverse ($ox^{'}y^{'}z^{'}$,Fig. S1(b)) propagation so that light always propagates toward the positive $z(z^{'})$ direction. Using this convention, the off-diagonal elements will acquire a minus sign, as shown below

$$J(\hat{k}) = \begin{pmatrix} A & B \\ C & D \end{pmatrix}; \qquad J(-\hat{k}) = \begin{pmatrix} A & -C \\ -B & D \end{pmatrix} \tag{5}$$

1.3 Geometric symmetries

Any geometric symmetry of the *system* imposes constraints on the form of the Jones matrix.

$$SJS^{-1} = J \tag{6}$$

where S is some spatial symmetry operation. A comprehensive classification can be found in (26).

Importantly, we emphasize the difference between the symmetries of the *structure* and the *system*. The latter contains both the structure and the light beam. The key distinction is whether or not the symmetry operation alters the light propagation direction $\hat{k}$. If a symmetry operation S leaves not only the structure but also the original propagation direction $\hat{k}$ unchanged, i.e. $S\hat{k} = \hat{k}$, then we say S is a symmetry of the system, and equation 6 holds. If S is a symmetry of the structure but $S\hat{k} \neq \hat{k}$, then equation 6 needs to be modified as

$$SJ(\hat{k})S^{-1} = J(S\hat{k}) \tag{7}$$

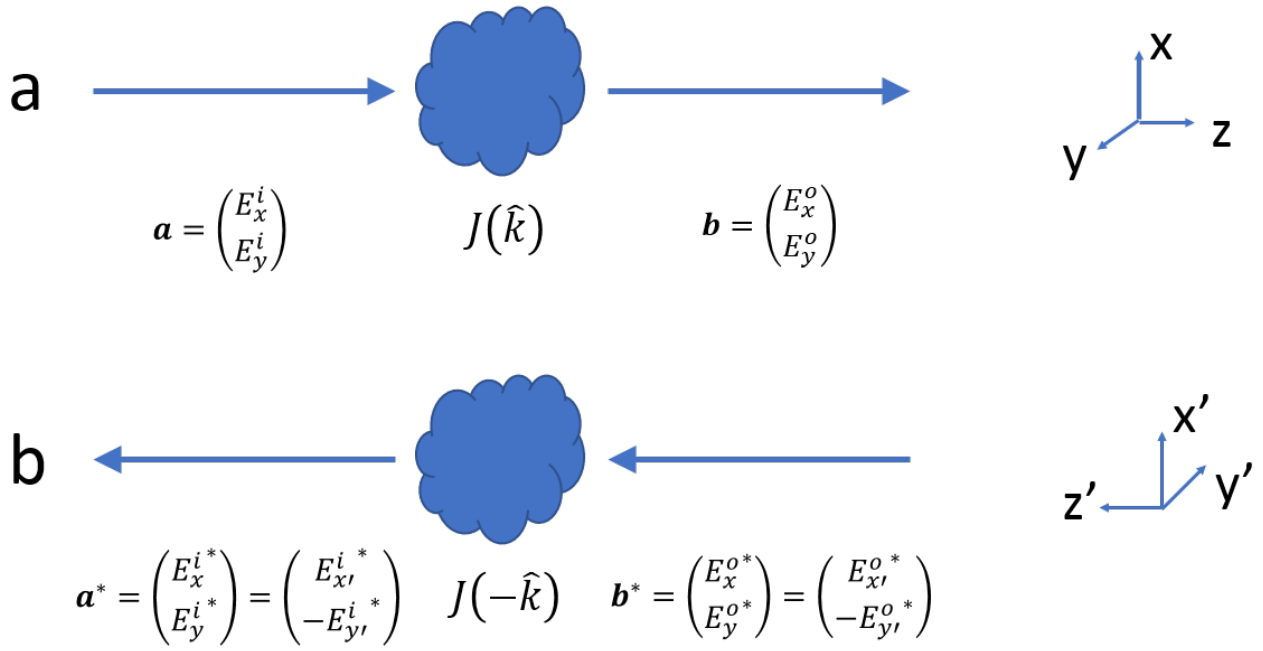

Figure S1: Reciprocity in unitary optical systems. (a) Forward ($\hat{k}$) propagation: the incident polarization state denoted by **a** is transformed into **b** at the output. (b) The reciprocal situation is given by phase conjugating the polarization state ($\mathbf{b} \to \mathbf{b}^*$), as well as reversing the propagation direction ($\hat{k} \to -\hat{k}$). Reciprocity requires that the transmitted polarization state should be the phase conjugate of that in the forward propagation case, i.e. ($\mathbf{a} \to \mathbf{a}^*$). Note that usually two different sets of coordinate systems $oxyz$ and $ox'y'z'$ are used for the forward and backward propagation.

Equation 7 links the Jones matrices for different propagation directions, but by itself does not directly impose any symmetry constraint on $J(\hat{k})$. Therefore, in general, the symmetry of the *structures* does not necessarily imply any symmetry of the Jones matrix of the *system* at an oblique incident angle. In fact, even highly symmetric structures can be slightly elliptically birefringent at some oblique incident angles. However, these effects are typically small and uncontrollable.

At normal incidence, the geometrical symmetries of the structures usually directly dictate the form of the Jones matrices. Some symmetry operations such as rotations around the z axis ($C_{n,z}$) and reflections with respect to the xz or yz plane (M_{xz}, M_{yz}) leave the light beam propagation direction unchanged, and therefore becomes a symmetry of the system, restricting the eigen-polarization states to be either linearly or circularly polarized. Other symmetries such as rotations around x or y axis ($C_{n,x}, C_{n,y}$) and reflections with respect to the zy plane (M_{xy}) transforms $\hat{k}$ into $-\hat{k}$, and can be combined with the reciprocity condition (equation 5) to derive the restrictions on the allowable Jones matrices (26).

Table S1 summarizes some of the key conclusions.

Unitarity	$J^\dagger J = 1$
Reciprocity	$J(-\hat{k}) = (J(\hat{k}))^T$ (in global coordinates)
Geometric symmetries	$SJ(\hat{k})S^{-1} = J(S\hat{k})$

Table S1: Symmetry requirements for Jones matrices

2 Design and Optimization

2.1 Symmetry considerations

The cross-sectional shape of our freeform design does not have any symmetry. However, there remain three constraints on the form of the Jones matrix: (approximate) unitarity, reciprocity, and approximate M_{xy} symmetry of the structure (mirror symmetry with respect to the xy plane). The latter results from the fact that the structures have vertical sidewalls and that the effect of the substrate is typically small.

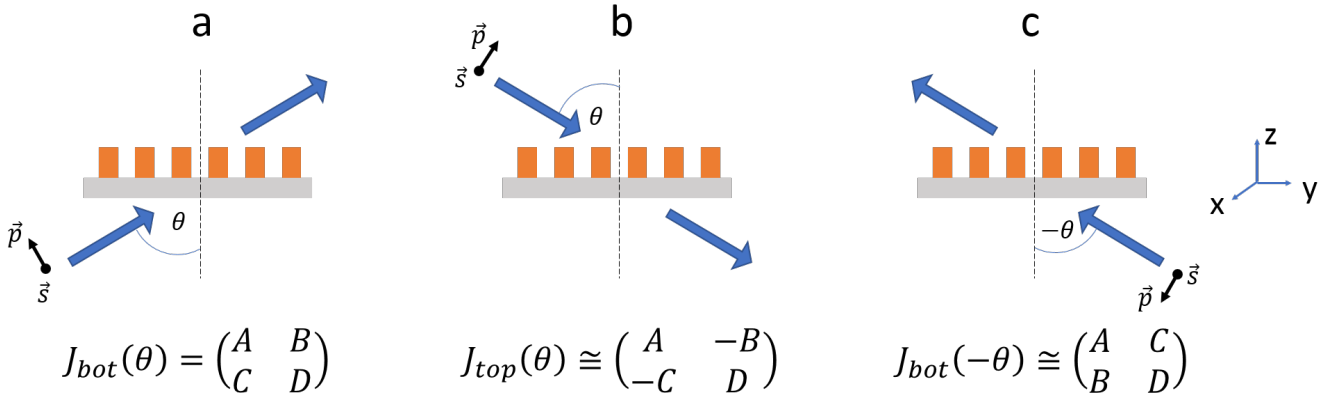

Figure S2: Symmetry considerations in metasurface design. Structures with vertical sidewalls are approximately mirror symmetric with respect to the xy plane (M_{xy}) if the effect of the substrate is small. In this case, the approximate M_{xy} symmetry connects the Jones matrices for incidence (a) from the bottom $J_{bot}(\theta)$ and (b) from the top $J_{top}(\theta)$. Furthermore, $J_{top}(\theta)$ is linked to $J_{bot}(-\theta)$ through reciprocity. The local (sp) coordinate systems used to define the Jones vectors and Jones matrices are shown.

According to equation 7, for a general incident angle θ, the M_{xy} symmetry requires that

$$J_{top}(\theta) \simeq M_{xy} J_{bot}(\theta) M_{xy}^{-1} = \begin{pmatrix} A & -B \\ -C & D \end{pmatrix} \quad \text{where} \quad M_{xy} = \begin{pmatrix} 1 & 0 \\ 0 & -1 \end{pmatrix}$$

Here the subscript *top* and *bot* corresponds to incidence from the top (air) and the bottom (substrate) side respectively (Fig. S2). The Jones matrices are written in local sp coordinate systems. In addition, reciprocity links $J_{top}(\theta)$ and $J_{bot}(-\theta)$ according to equation 5, yielding

$$J_{bot}(-\theta) \simeq \begin{pmatrix} A & C \\ B & D \end{pmatrix}$$

Therefore we have

$$J(\theta) \simeq J(-\theta)^T \tag{8}$$

where the subscript has been omitted as the incidence is from the same side.

In addition, if the Jones matrix is unitary, then $J(\theta) \simeq J(-\theta)^T$ implies that the eigenstates at $\pm\theta$ are complex conjugate to each other, i.e. $|\lambda_+(-\theta)\rangle \simeq |\lambda_+^*(\theta)\rangle$ and $|\lambda_-(-\theta)\rangle \simeq |\lambda_-^*(\theta)\rangle$. In particular, this requires that at normal incidence the eigenstates have to be real, which physically means that the eigen-polarization states are linearly polarized. Therefore, in the optimization we require the device to have the desired elliptical birefringence at oblique angles of incidence, but remain linearly birefringent at normal incidence to obey the physical constraint.

2.2 Figure of Merit (FOM)

As a proof-of-principle demonstration, we would like to convert a horizontally polarized incident light $|H\rangle$ into 45° oriented linear polarization $|45°\rangle$ and right circular polarization $|RCP\rangle$ at ±60° respectively, while preserving the polarization states at normal incidence. The figure of merit (FOM) is defined as the following

$$FOM = \text{maxmin}\{|\langle RCP|J(-\theta_0)|H\rangle|^2, |\langle H|J(0°)|H\rangle|^2, |\langle 45°|J(\theta_0)|H\rangle|^2\}$$

where $\theta_0 = 60°$, and maxmin means maximizing the minimum of the polarization conversion efficiencies at different design angles.

We argue that the above-defined FOM automatically guarantees elliptical birefringence at $\pm 60°$ incident angles. Due to the condition $J(\theta) \simeq J(-\theta)^T$ (SI section 2.1), the requirement that $J(-\theta_0)|H\rangle \rightarrow |RCP\rangle$ and $J(\theta_0)|H\rangle \rightarrow |45°\rangle$ is equivalent to

$$J(\theta_0)|H\rangle \rightarrow |45°\rangle, \qquad J(\theta_0)^T|H\rangle \rightarrow |RCP\rangle \tag{9}$$

Applying the unitary condition $J(\theta_0)^T = (J(\theta_0)^{-1})^*$,the second part can be rewritten as

$$\begin{aligned} & (J(\theta_0)^{-1})^*|H\rangle \rightarrow |RCP\rangle \\ \Leftrightarrow \quad & J(\theta_0)^{-1}|H\rangle \rightarrow (|RCP\rangle)^* = |LCP\rangle \\ \Leftrightarrow \quad & J(\theta_0)|LCP\rangle \rightarrow |H\rangle \end{aligned}$$

Therefore, equation (9) becomes

$$J(\theta_0)|H\rangle \rightarrow |45°\rangle, \qquad J(\theta_0)|LCP\rangle \rightarrow |H\rangle \tag{10}$$

Using the geometrical representation, we know that $J(\theta_0)$ induces a rotation on the Poincare sphere. To simultaneously satisfy both requirements in equation (10), the Poincare sphere rotation axis for $J(\theta_0)$ must be equidistant from $|H\rangle$, $|LCP\rangle$ and $|45°\rangle$ (Fig. S3). One can see immediately that this corresponds to the case of elliptical birefringence. Therefore, our definition of FOM automatically guarantees having elliptical birefringence at $\theta = \pm 60°$.

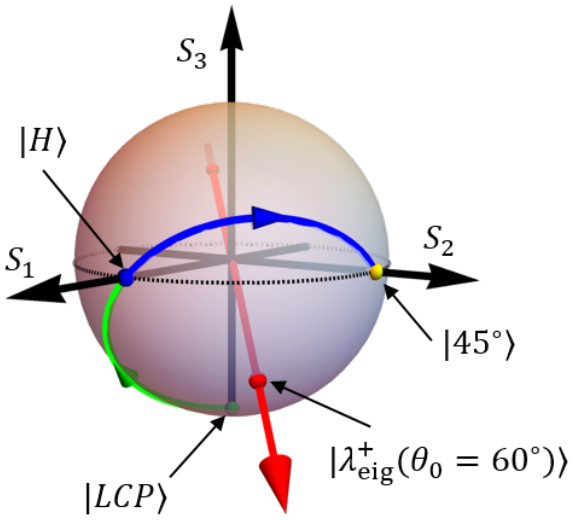

Figure S3: Poincare sphere representation for $J(\theta_0 = 60°)$. The red arrow corresponds to the polarization state rotation axis, which is determined by the eigenstate $|\lambda_{\text{eig}}\rangle$. The $|LCP\rangle$ (green dot), $|H\rangle$ (blue dot), and $|45°\rangle$ (yellow dot) states can be connected through rotations around this axis.

2.3 Optimization procedure

The optimization procedure is similar to that in (23). We used the open source Rigorous Coupled Wave Analysis (RCWA) solver - RETICOLO for electromagnetic simulation (34). The optimization is implemented using Matlab built-in optimization toolbox. A random continuous initial refractive index pattern is generated without preset symmetry constraints. For each iteration, forward and adjoint simulations are performed for $\theta = 0°, \pm 60°$ to compute the gradient and to update the refractive index profile. Robustness is built in by considering simultaneously the diluted, intermediate and eroded pattern. Gaussian filters are used to remove small sharp features and to achieve a connected pattern. A hyperbolic tangent function is applied to gradually push the continuous refractive index profile to discrete structures which contain only air and silicon. The optimization is performed iteratively and typically converges within 300 iterations.

3 Simulation results

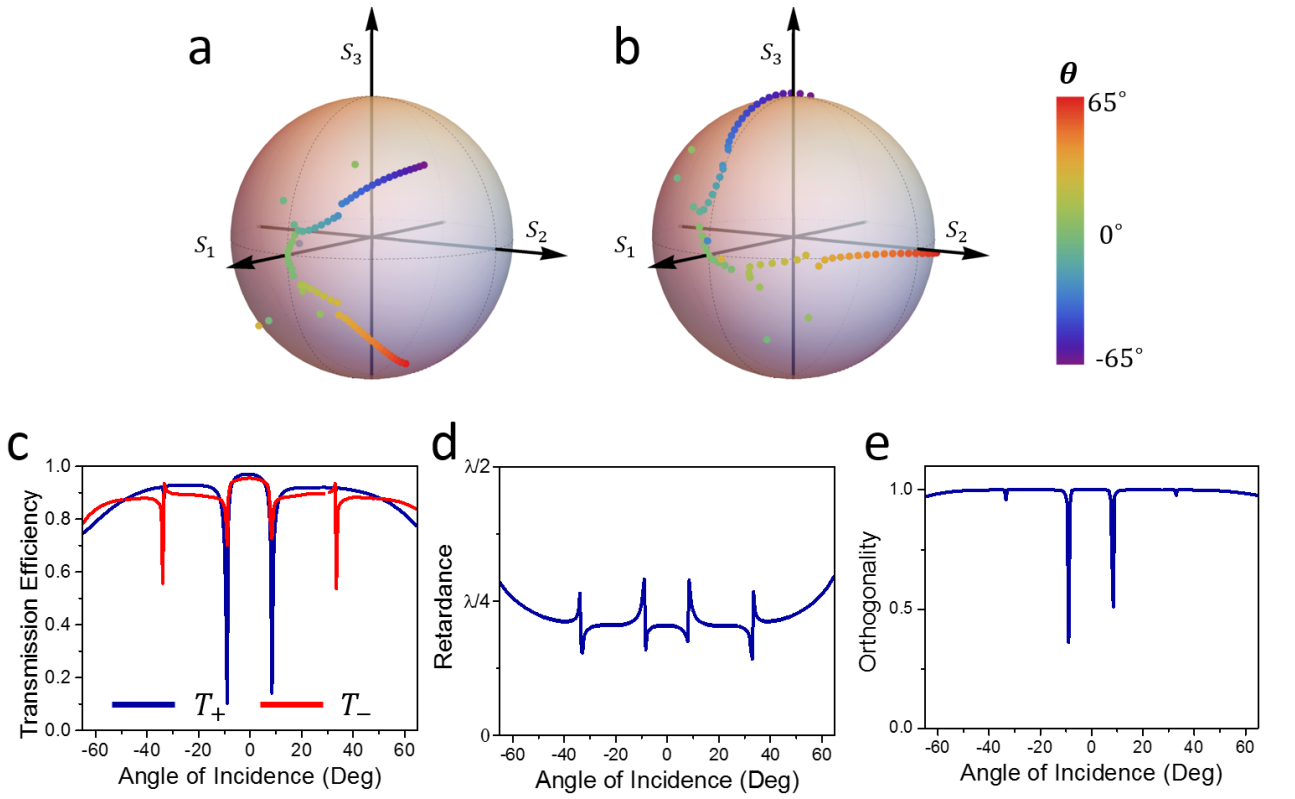

Figure S4: Simulation results for the original design. (a) Simulated eigen-polarization state for various angles of incidence. (b) Simulated output polarization states (for $|H\rangle$ incidence) as a function of angles of incidence. (c) Simulated transmission efficiency for the two eigen-polarization states. (d) Simulated retardance. (e) Simulated orthogonality of the eigen-polarization states.

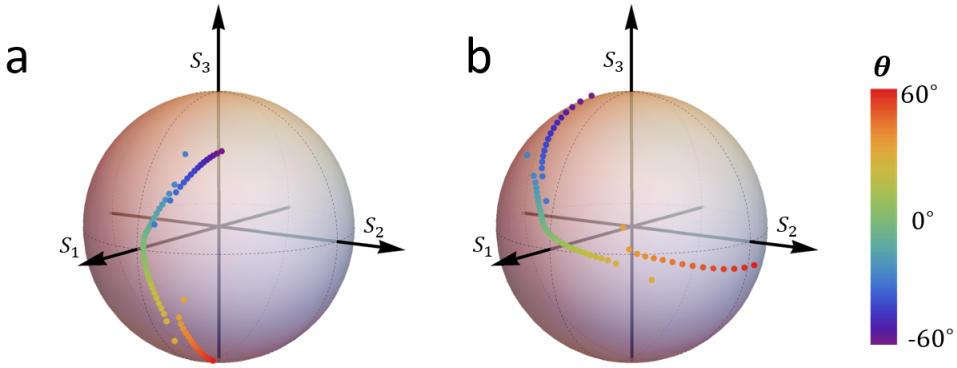

Figure S5: Simulation results considering possible fabrication errors. The simulated structure is dilated by 10 nm in the cross-sectional shape, and also 100 nm shorter in height compared to the original design. (a) Simulated eigen-polarization states for various angles of incidence. (b) Simulated output polarization states (for $|H\rangle$ incidence) as a function of angles of incidence.

3.1 Simulation results for the optimized design

Figure S4 shows the simulated eigen-polarization states and output polarization states for various angles of incidence, as well as the transmission, retardance and orthogonality information.

3.2 Simulation results considering possible fabrication errors

The difference between the simulation and measurement may be explained by inaccurate material refractive indices and fabrication imperfections. Although we implemented robustness control in the optimization considering structure dilation and erosion, in reality, the fabrication errors are much more diverse and complex. In figure S5, we simulated a device that is not only dilated by 10 nm in the cross-sectional shape, but also 100 nm shorter in height (H=1400 nm) compared to the original design. The simulation results resemble the measurement data, suggesting that the deviation might result from a combination of lateral size and height difference.

3.3 Comparison with the forward design

In theory, the structure does not have to be freeform to exhibit elliptical birefringence, as long as it avoids the symmetry constraints discussed in SI sec.1. However, without optimization, these effects are usually small and uncontrollable. Here we simulated a class of asymmetric U shape structures (Fig. S6). We did a parameter sweep of the lengths and widths (labeled in Fig. S6) using the traditional forward design method. The simulation results for the best design is shown in Figure S6(b). One can see that the eigen-polarization states become slightly elliptically polarized at oblique angles of incidence, however, the change is much smaller than that obtained with topological optimization.

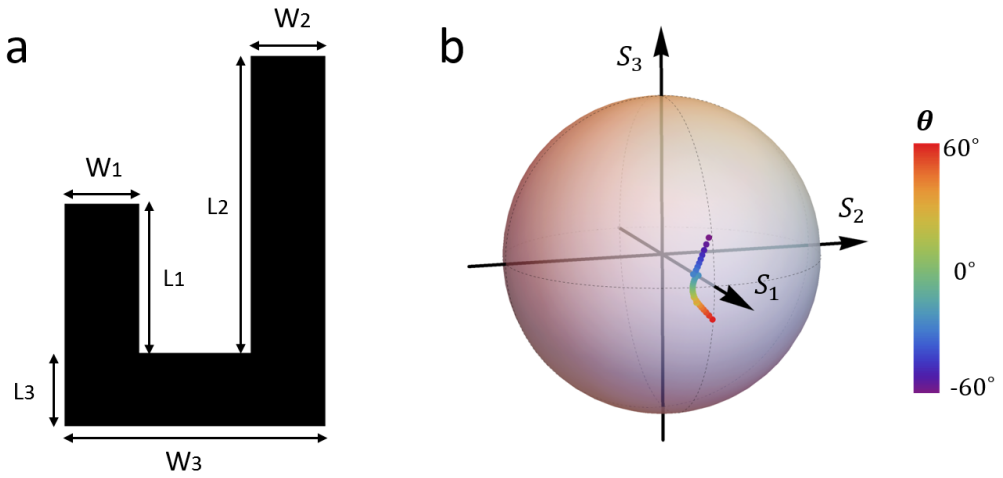

Figure S6: Simulation results for the forward design. (a) The cross-sectional pattern is an asymmetric U shape. The structure height and unit cell size is fixed at 1500 nm and 600 nm respectively. (b) Simulated eigen-polarization states for various angles of incidence. The eigen-polarization states become slightly elliptically polarized at oblique angles of incidence, however, the change is much smaller than that obtained with topological optimization. In this design, $W_1 = W_2 = L_3 = 100$ nm, $W_3 = 340$ nm, $L_1 = 200$ nm, $L2 = 400$ nm.

4 Polarimetric measurement and data analysis

4.1 Jones v.s. Mueller calculi

Two formalisms exist to describe the polarization states of light and the polarization effects of optical elements: Jones calculus and Mueller calculus (Table S2) (13). Disregarding coherent wave superposition, for fully polarized light and non-depolarizing optical elements, the two formalisms provide equivalent information (up to an overall phase) and can be converted from one to another.

In most of our analysis, we use the Jones formalism as it is more compact and physically more intuitive. However, since the Jones vector and Jones matrix are complex quantities, they are not directly measurable. Therefore, in the experiments, we measure the Stokes vectors and Mueller matrices, as they consist of real quantities that can be directly determined via intensity measurements.

Jones calculus	**Mueller calculus**
Jones vector: $\|\lambda\rangle = e^{i\phi}\begin{pmatrix}\cos\Psi\\ e^{i\delta}\sin\Psi\end{pmatrix}$	Stokes vector: $S = \begin{pmatrix}1\\ \cos 2\Psi\\ \sin 2\Psi\cos\delta\\ \sin 2\Psi\sin\delta\end{pmatrix}$
Jones matrix: $\|\lambda_{out}\rangle = J\|\lambda_{in}\rangle$ $J = \begin{pmatrix}\rho_{xx}e^{i\phi_{xx}} & \rho_{xy}e^{i\phi_{xy}}\\ \rho_{yx}e^{i\phi_{yx}} & \rho_{yy}e^{i\phi_{yy}}\end{pmatrix}$	Mueller matrix: $S_{out} = MS_{in}$ $M = \begin{pmatrix}m_{00} & m_{01} & m_{02} & m_{03}\\ m_{10} & m_{11} & m_{12} & m_{13}\\ m_{20} & m_{21} & m_{22} & m_{23}\\ m_{30} & m_{31} & m_{32} & m_{33}\end{pmatrix}$

Table S2: Jones & Mueller calculi

Conversion formulae	
Jones matrix to Mueller matrix	$M = U(J\otimes J^*)U^{-1}, \quad U = \frac{1}{\sqrt{2}}\begin{pmatrix}1 & 0 & 0 & 1\\ 1 & 0 & 0 & -1\\ 0 & 1 & 1 & 0\\ 0 & i & -i & 0\end{pmatrix}$
Mueller matrix to Jones matrix	$\rho_{xx} = \frac{1}{\sqrt{2}}\sqrt{m_{00}+m_{01}+m_{10}+m_{11}}$ $\rho_{xy} = \frac{1}{\sqrt{2}}\sqrt{m_{00}-m_{01}+m_{10}-m_{11}}$ $\rho_{yx} = \frac{1}{\sqrt{2}}\sqrt{m_{00}+m_{01}-m_{10}-m_{11}}$ $\rho_{yy} = \frac{1}{\sqrt{2}}\sqrt{m_{00}-m_{01}-m_{10}+m_{11}}$ $\phi_{xy}-\phi_{xx} = \arctan(\frac{-m_{03}-m_{13}}{m_{02}+m_{12}})$ $\phi_{yx}-\phi_{xx} = \arctan(\frac{m_{30}+m_{31}}{m_{20}+m_{21}})$ $\phi_{yy}-\phi_{xx} = \arctan(\frac{m_{32}-m_{23}}{m_{22}+m_{33}})$

Table S3: Conversion formulae

4.2 Measurement setup

To fully characterize the device's polarization response, dual-rotating retarder Mueller matrix polarimetry (30) was performed at various angles of incidence (Fig. S8). The setup has five sections: the laser source, the polarization state generator (PSG), the metasurface sample (mounted on a rotation stage), the polarization state analyzer (PSA), and the detector. An iris and a lens are used to concentrate light on the sample. The focused beam has a divergence angle of around 0.3°, smaller than the angular resolution of the rotation stage (1°). Both the PSG and PSA consist of a fixed linear polarizer and a rotating quarter waveplate. Here the two polarizers are aligned parallel to the horizontal direction and the two waveplates are rotated in angular increments of five-to-one. The PSG prepares a set of polarization states, which then pass through the sample and get analyzed by the PSA. Although Mueller polarimetry already provides complete information regarding the polarization properties of the sample, for illustration purposes, we also performed separate Stokes polarimetry to measure the output polarization for a fixed input polarization state This is done using the same setup but without the quarter waveplate in the PSG so that the incident polarization is fixed to be horizontal linear polarization.

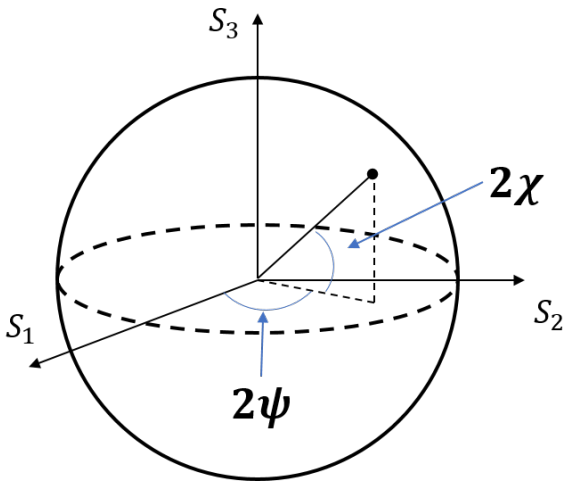

Figure S7: Poincare sphere. ψ and χ correspond to the orientation and ellipticity angle of the polarization ellipse.

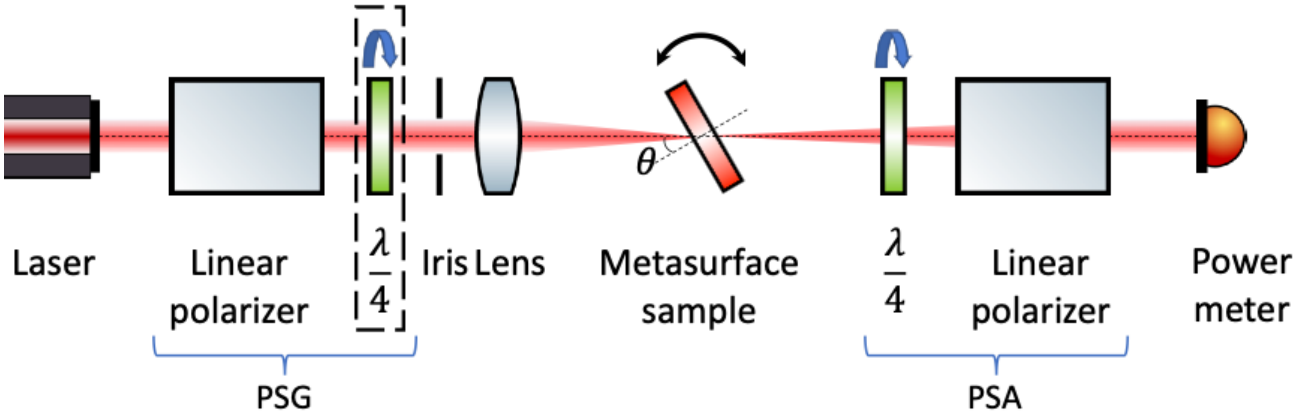

Figure S8: Measurement setup. The measurement setup consists of the light source, the polarization state generator (PSG), the sample mounted on a rotation state, the polarization state analyzer (PSA) and the detector.

4.3 Measurement data analysis

At each angle, each Mueller matrix polarimeter takes 16 intensity measurements. For the qth measurement, the polarization generator produces a beam with Stokes vector S_q. The beam transmits through the sample and is analyzed with an analyzer vector A_q (i.e. the outgoing beam is projected onto the polarization state A_q). The measured intensity I_q is given by

$$I_q = A_q^T M S_q = \sum_i \sum_j a_{q,i} s_{q,j} m_{i,j}$$

Here $a_{q,i}$ and $s_{q,j}$ are components of the A_q and S_q, and are determined by the polarization generator and analyzer configuration (i.e. the orientation of the quarter waveplates). Each intensity measurement results in a linear constraint on the matrix elements of M. With 16 linearly independent equations, the Mueller matrix, which has 16 real elements, can be obtained via matrix inversion.

The measured Mueller matrices are then converted to Jones matrices using the formula in Table S2 (13). The eigen-vectors and eigenvalues are computed via matrix diagonalization. The phase difference of the eigenvalues yields the retardance. Note that the eigenvalues are complex amplitudes, so to obtain intensity we take the square of their absolute values. Transmission efficiency is computed by normalizing the "eigen"-intensity obtained with the sample to that without the sample.

5 Mode analysis

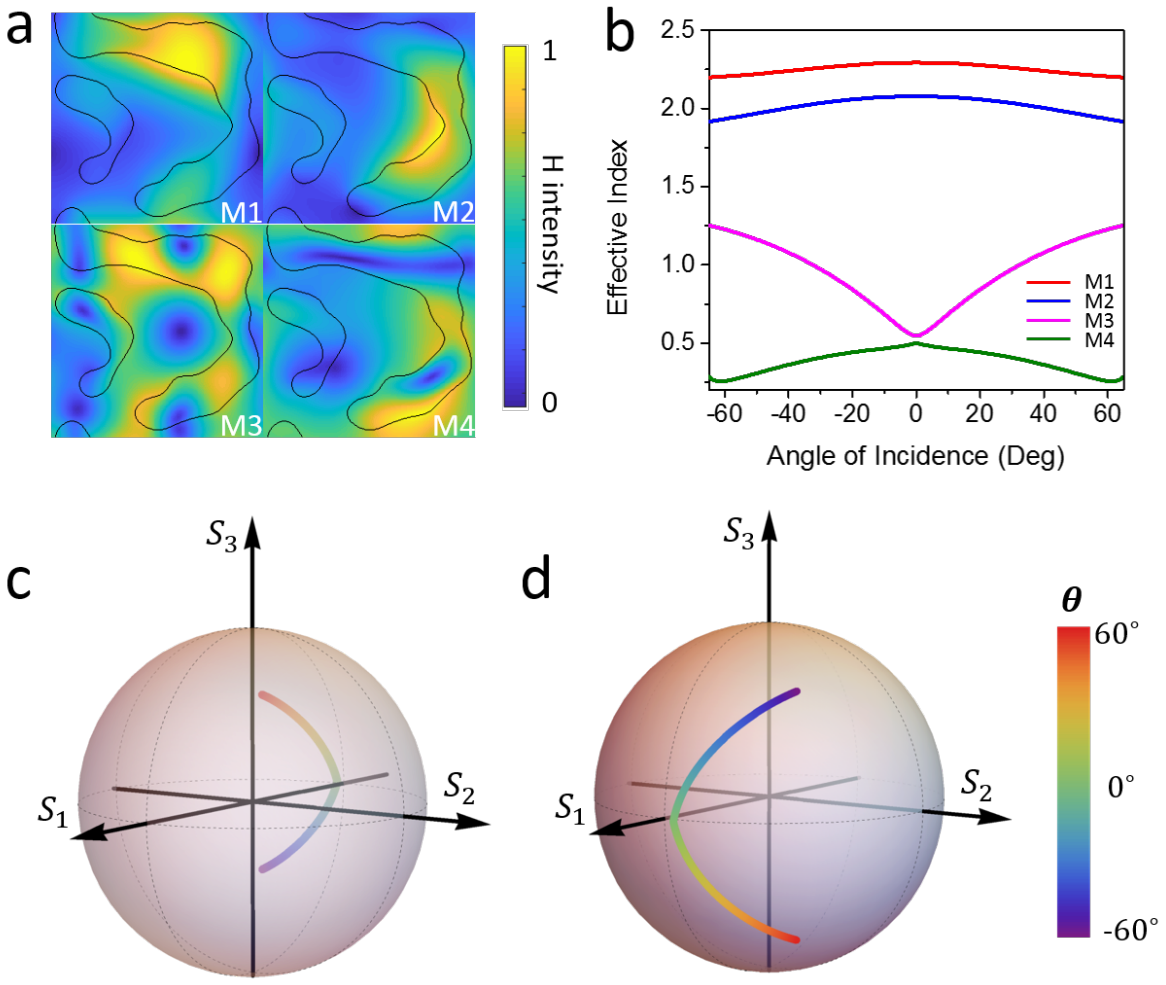

Figure S9: Mode analysis. (a) Magnetic field intensity profiles of propagating Bloch modes. The mode profiles are computed for normal propagation direction ($\hat{k} = 0$). (b) Effective refractive indices of the Bloch modes. (c-d) Far-field polarization states of the two lowest order Bloch modes, M1 (c) and M2 (d). Their angular response agrees quantitatively with that of the device's eigen polarization states (Fig. 5 (b-c)), indicating that they are the main contributing Bloch modes away from resonances.

To investigate the physical mechanism of the observed unconventional polarization response, we analyzed the Bloch modes (31) supported in the metasurface layer. Inside the nanostructures, the fields expand into a basis of Bloch modes, the eigen-modes of the nanostructure layer. At the interfaces - the Bloch modes are partially transmitted and reflected. Although the Bloch modes are eigenmodes inside the nanostructure, in general they mix together upon reflection. The metasurface can be effectively treated as a Fabry-Perot cavity of the Bloch modes. When incident light impinges on the metasurface, it couples to the Bloch modes, which bounce between the interfaces and eventually couple out to free space, contributing either to the transmitted or reflected light. The optical response of the metasurface is ultimately determined by the characteristics and scattering dynamics of these Bloch modes.

Four propagating Bloch modes are identified in our structure (Fig. S9(a)). Among them, the first two Bloch modes (M1 and M2) dominate the overall optical response, and the other two higher order modes are responsible for the guided mode excitation at the resonances. The dominating role of the two lowest order modes becomes evident as one compare their far field polarization states (Fig. S9(c-d)) with the eigen-polarization states of the metasurface (Fig. 4(b-c)). The overall trend agrees qualitatively, indicating that they are the main contributions to the observed birefringent response.